Table of contents

Supplementary Note 1. The modified Williamson-Hall (MWH) method

Dislocation densities were calculated using the modified Williamson-Hall (MWH) method based on *ex-situ* and *in-situ* HEXRD measurements [1,2]. The shift in the diffraction peak ΔK related to the full width at half maximum (FWHM) is expressed as follows [1,2]:

$$\Delta K=\frac{0.9}{D}+\left(\frac{\pi A^2 b^2}{2}\right)^{1/2}\rho^{1/2}K\overline{C}^{1/2}+O(K^4\overline{C}^2) \quad (1)$$

Where D is the grain size, $A=R_e\sqrt{\rho}$ is a constant ranging from 1 to 2 (with R_e as the effective outer cut-off radius of dislocations), and ρ is the dislocation density. The Burgers vector of the perfect dislocation is b=0.250 nm. The diffraction vector is $K=2\sin\theta/\lambda$, where θ is the diffraction angle and λ is the X-ray wavelength. O represents a negligible higher-order term of $K\overline{C}^{1/2}$. The dislocation contrast factor $\overline{C}$ is given by:

$$\overline{C}=\overline{C}_{h00}(1-qH^2) \quad (2)$$

Where $\overline{C}_{h00}$ and q are constants determined by the elastic constants of the crystal, and H represents the fourth-order ratio derived from the Miller indices h, k, and l:

$$H^2=\frac{h^2k^2+h^2l^2+k^2l^2}{(h^2+k^2+l^2)^2} \quad (3)$$

The constants $\overline{C}_{h00}$ and q are calculated using the following equations:

$$\overline{C}_{h00}=a_1\left[1-exp\left(-\frac{A_i}{b_1}\right)\right]+c_1A_i+d_1 \quad (4)$$

$$q=a_2\left[1-\exp\left(-\frac{A_i}{b_2}\right)\right]+c_2A_i+d_2 \quad (5)$$

Where $A_i=2c_{44}/(c_{11}-c_{12})$ represents the elastic anisotropy, and the elastic constants are c_{11}=260 GPa, c_{12}=131 GPa, and c_{44}=106 GPa [3]. The constants a_1, b_1, c_1, d_1, a_2, b_2, c_2, and d_2 are associated with the anisotropic elastic constants and dislocation character. The ratio of edge-to-screw dislocations

is assumed to be 1, and the values of $\overline{C}_{h00}$ and q are determined as 0.2070 and 1.5137, respectively. The relationship between ΔK and FWHM (here denoted as β) of different lattice diffraction peaks obtained from XRD profiles is given by:

$$\Delta K = \frac{2\beta \cos\theta}{\lambda} \tag{6}$$

Supplementary Note 2. Density functional theory (DFT)/Monte Carlo (MC) simulation

The hybrid density functional theory/Monte Carlo (DFT/MC) method was utilized to investigate the energy evolution of the CRA alloy both prior to and following Mo segregation. A 100-atom supercell was designed to model the chemical disorder, preserving a composition ratio of Fe:Co:Mo as 5:4:1. This approach effectively captures the intricate atomic interactions and chemical inhomogeneities, providing detailed insights into the energetic effects of Mo segregation on the alloy's microstructure.

Supplementary Note 3. The extended Kocks-Mecking plot

Based on Schoeck's principle [4], Van Liempt and Sietsma derived an equation that describes the entire pre-yield stage of the extended Kocks-Mecking plot [5,6]:

$$\Theta^{\mathrm{pre}} = \frac{M^2 E s^3 \sqrt{1-s^2}}{M^2 s^3 \sqrt{1-s^2} + \rho \bar{L}^2 (1+\nu)(s - \sqrt{1-s^2}\arcsin(s))} \tag{7}$$

This equation allows us to calculate the dislocation density ρ and the average dislocation segment lengths $\bar{L}$ by fitting the work-hardening rate Θ as a function of the flow stress σ. Here, M is the Taylor factor, E is the Young's modulus, ν is Poisson's ratio (ν=0.3). The dimensionless stress parameter s is given by:

$$s = \frac{\sigma}{\sigma_y} = \frac{\sigma \bar{L}}{MGb} \tag{8}$$

Where G is the shear modulus, b is the Burgers vector, and σ_y is the yield strength.

Supplementary Note 4. Discrete dislocation dynamics (DDD) simulation

The DDD simulations were performed using the open-source ParaDiS code, developed by Lawrence Livermore National Laboratory. The simulation domain was a cubic box with dimensions of 0.25 μm×0.25 μm×0.25 μm, employing periodic boundary conditions on all surfaces. To replicate the alloy's microstructure, 99 screw dislocation lines were randomly distributed within the body-centered cubic (BCC) matrix, corresponding to a dislocation density of 2.3×10^{15} m^{-2}. A strain rate of 1×10^{6} s^{-1} was applied, based on prior DDD simulations and the computational constraints associated with simulation time.

To explore the mesoscale impact of elemental segregation on the alloy's properties, the lattice strain field induced by segregation was incorporated into the discrete dislocation dynamics (DDD) simulation using random field theory. High-resolution scanning transmission electron microscopy (HRSTEM) imaging combined with geometric phase analysis (GPA) was employed to characterize the lattice strain fields in regions with and without elemental segregation. The experimentally obtained strain field was fitted to a fractal function and integrated into the DDD code, enabling simulations that capture the influence of segregation-induced lattice strain on dislocation dynamics and alloy performance.

Supplementary Note 5. Strengthening contributions of CR and CRA alloys

The strengthening mechanisms of the CR and CRA alloys were quantitatively analyzed, with the yield strength (σ_y) expressed as the sum of friction stress (σ_0), solid solution strengthening ($\Delta\sigma_{ss}$), dislocation strengthening ($\Delta\sigma_{dis}$), and grain boundary strengthening ($\Delta\sigma_{gb}$):

$$\sigma_y=\sigma_0+\Delta\sigma_{ss}+\Delta\sigma_{dis}+\Delta\sigma_{gb} \quad (9)$$

The friction stress (σ_0) was assumed to be 50 MPa [7]. Solid solution strengthening ($\Delta\sigma_{ss}$) arising from the critical resolved shear stress increment caused by solute atoms, was estimated using Fleischer's equation [8,9]:

$$\Delta\sigma_{ss}=\sum(\beta_i^2 X_{i,\alpha})^{1/2} \quad (10)$$

Here, β_i represents the strengthening constant associated with the lattice and modulus misfit of substitutional element i, and $X_{i,\alpha}$ is its atomic fraction in the matrix. The β_i values for Mo and Co were 2143, and 334, respectively [9,10].

Dislocation strengthening ($\Delta\sigma_{dis}$) was estimated using the Taylor hardening law [11,12]:

$$\Delta\sigma_{dis}=M\alpha\mu b\sqrt{\rho} \quad (11)$$

where M=2.908 is the Taylor factor [13], α=0.24 is an empirical constant [14], μ=77 GPa is the shear modulus of martensite [15,16], $b=\frac{\sqrt{3}}{2}a$=0.25 nm is the Burgers vector, and a=2.89 Å is the lattice constant obtained from synchrotron X-ray diffraction (HEXRD). The dislocation density (ρ) was determined using the modified Williamson–Hall (MWH) method, yielding values of 2.31×10^{15} and 4.08×10^{15} m^{-2} for the CRA and CR alloys, respectively.

Grain boundary strengthening ($\Delta\sigma_{gb}$) was described by the Hall–Petch relationship [17,18]:

$$\Delta\sigma_{gb}=\frac{k}{d^{1/2}} \quad (12)$$

where d is the average grain size determined via electron backscatter diffraction (EBSD), and k is the Hall–Petch constant, taken as 373 MPa $\mu m^{1/2}$ [7].

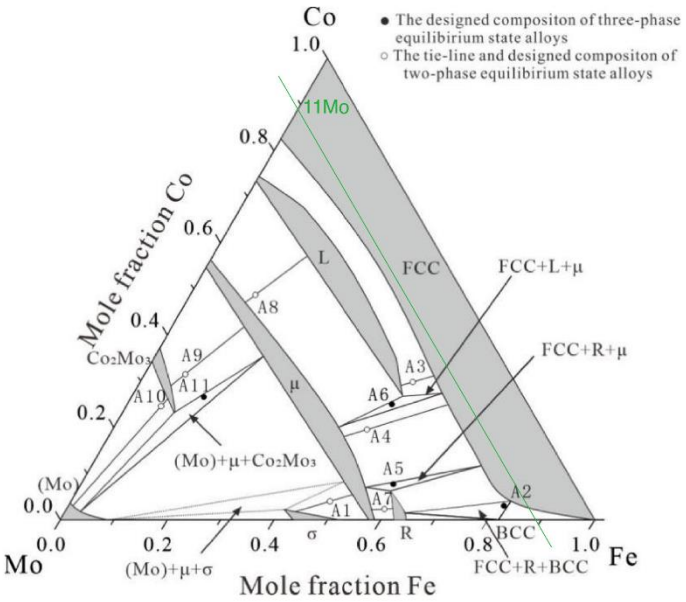

Supplementary Fig. 1 | Fe–Mo–Co isothermal section at 1350 °C [19]. The γ-FCC single-phase field directs composition selection; the green line marks 11 at. % Mo near the boundary of the FCC single-phase field.

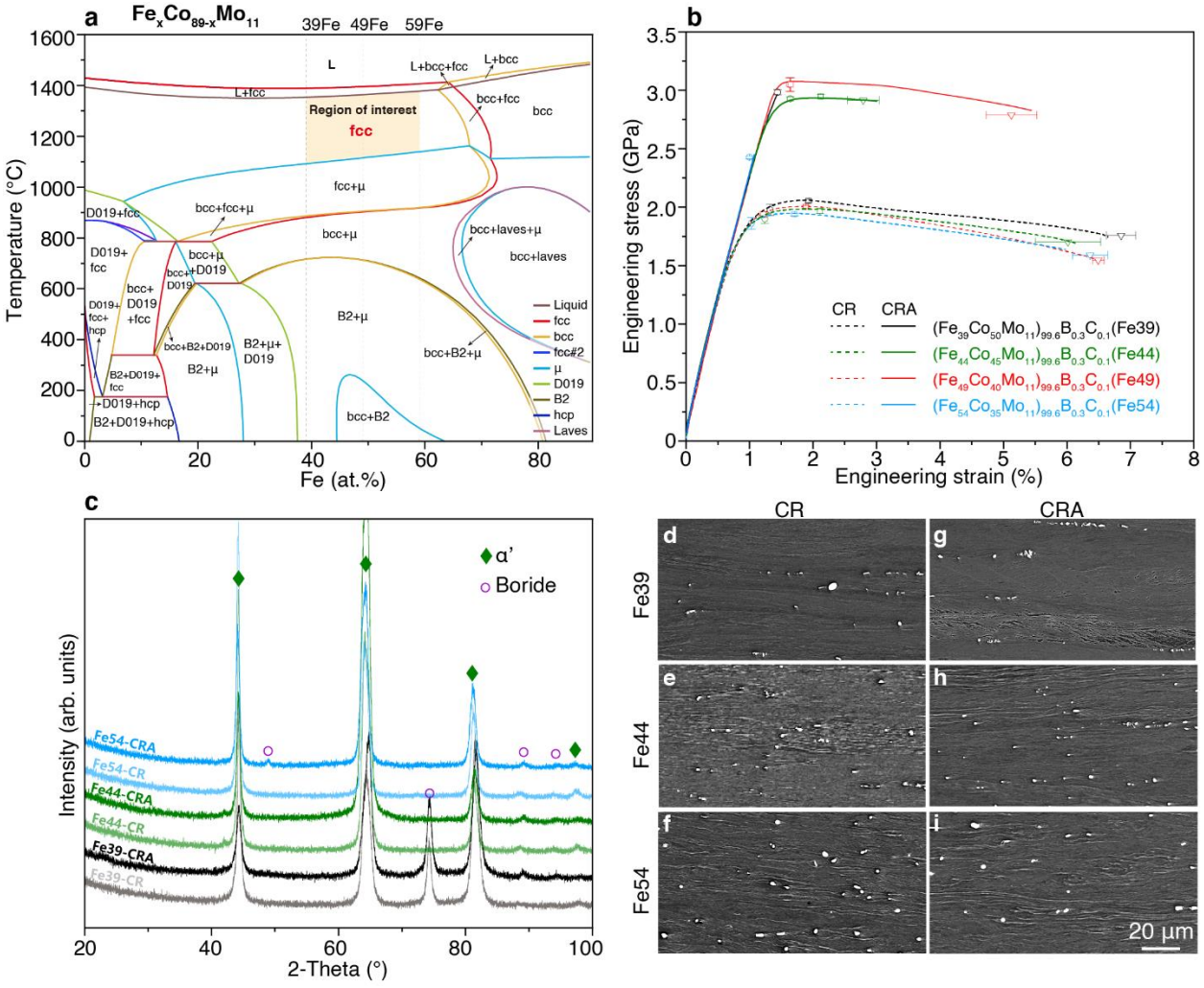

Supplementary Fig. 2 | Thermodynamic screening and down-selection of Fe–Co–Mo alloys. **a,** CALPHAD-predicted phase diagram of $Fe_xCo_{89-x}Mo_{11}$ pseudo-binary system. **b,** Room-temperature engineering stress-strain curves of $(Fe_{39}Co_{50}Mo_{11})_{99.6}B_{0.3}C_{0.1}$, $(Fe_{44}Co_{45}Mo_{11})_{99.6}B_{0.3}C_{0.1}$, $(Fe_{49}Co_{40}Mo_{11})_{99.6}B_{0.3}C_{0.1}$, and $(Fe_{54}Co_{35}Mo_{11})_{99.6}B_{0.3}C_{0.1}$ alloys after cold rolling (CR) and annealing (CRA). The data points and error bars represent the mean ± standard deviation (s.d.) taken from three independently tensile samples. **c,** XRD patterns of the alloys in CR and CRA conditions. **d-f, g-i** SEM micrographs of CR and CRA microstructures, respectively.

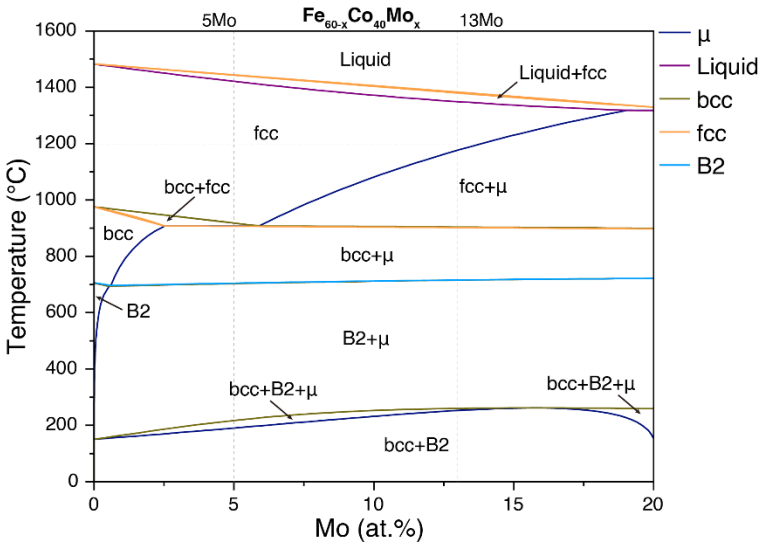

Supplementary Fig. 3 | CALPHAD-predicted phase diagram of the $Fe_{60-x}Co_{40}Mo_x$ system. Thermodynamic calculations were conducted to evaluate phase stability across the Fe–Co–Mo compositional range.

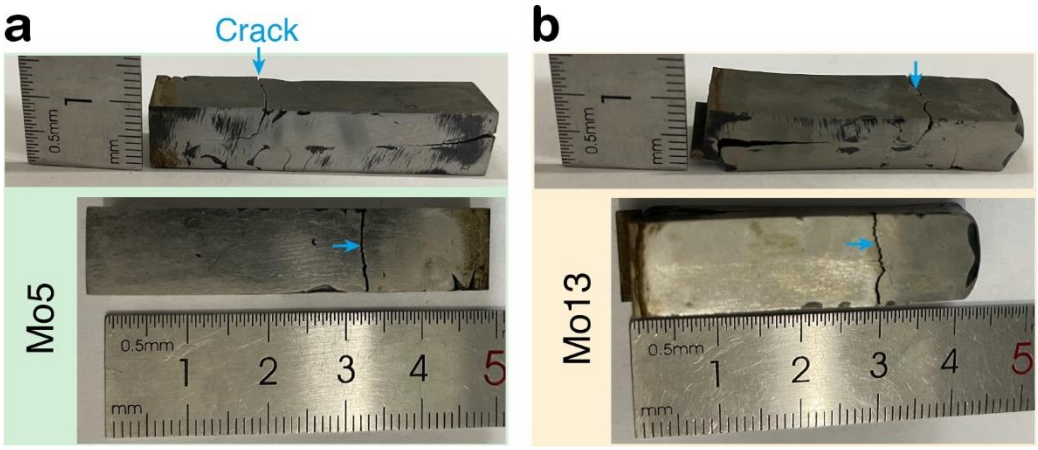

Supplementary Fig. 4 | Optical micrographs of the as-rolled low- and high-Mo alloys. Optical images of $(Fe_{55}Co_{40}Mo_5)_{99.6}B_{0.3}C_{0.1}$ and $(Fe_{47}Co_{40}Mo_{13})_{99.6}B_{0.3}C_{0.1}$ alloys after ~5% cold rolling, both exhibiting cracks that signal poor workability.

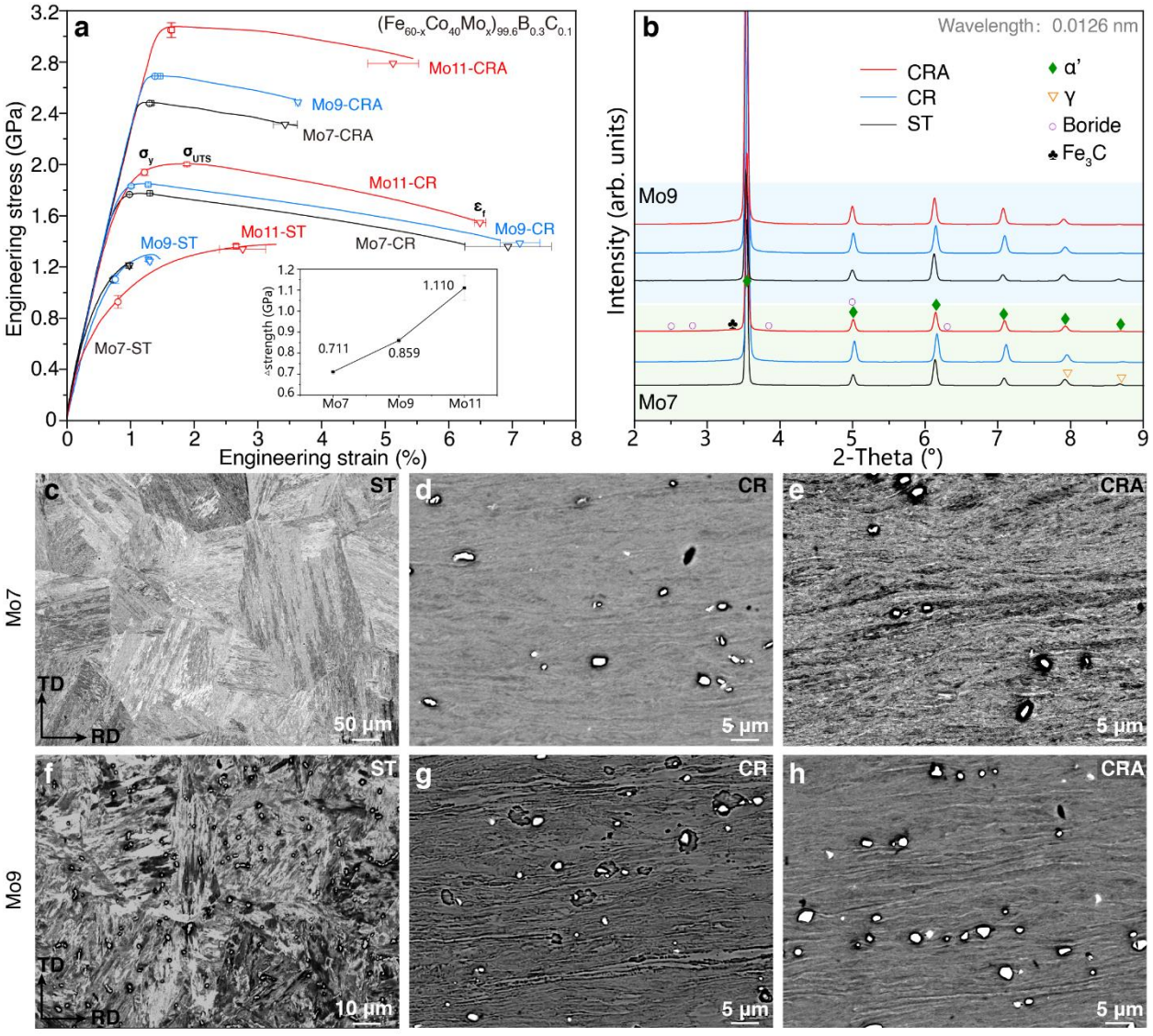

Supplementary Fig. 5 | Mechanical properties and microstructures of $(Fe_{60-x}Co_{40}Mo_x)_{99.6}B_{0.3}C_{0.1}$ alloys with varying Mo content (x = 7, 9, and 11 at.%, denoted as Mo7, Mo9, and Mo11). a, Room-temperature engineering stress–strain curves showing enhanced mechanical performance with increasing Mo content. ST, where the as-cast alloy was homogenized at 1200 °C for 2 h. The data points and error bars represent the mean ± standard deviation (s.d.) taken from three independently tensile samples. **b,** HEXRD patterns confirming that all alloys predominantly consist of a martensitic phase. **c–e**, SEM images of the Mo7 alloy,

and **f-g**, SEM images of the Mo9 alloy, revealing similar microstructures characterized by lath martensite and a minor fraction of boride precipitates.

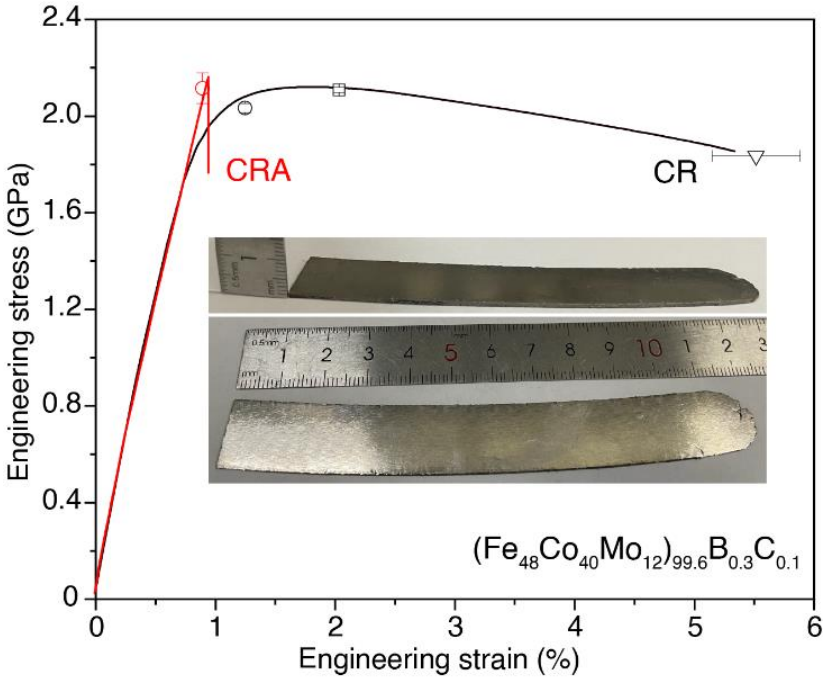

Supplementary Fig. 6 | Room-temperature engineering stress-strain curves of the $(Fe_{48}Co_{40}Mo_{12})_{99.6}B_{0.3}C_{0.1}$ alloy. The limited ductility of the annealed (CRA) alloy defines the upper Mo limit for usable ductility. The data points and error bars represent the mean ± standard deviation (s.d.) taken from three independently tensile samples.

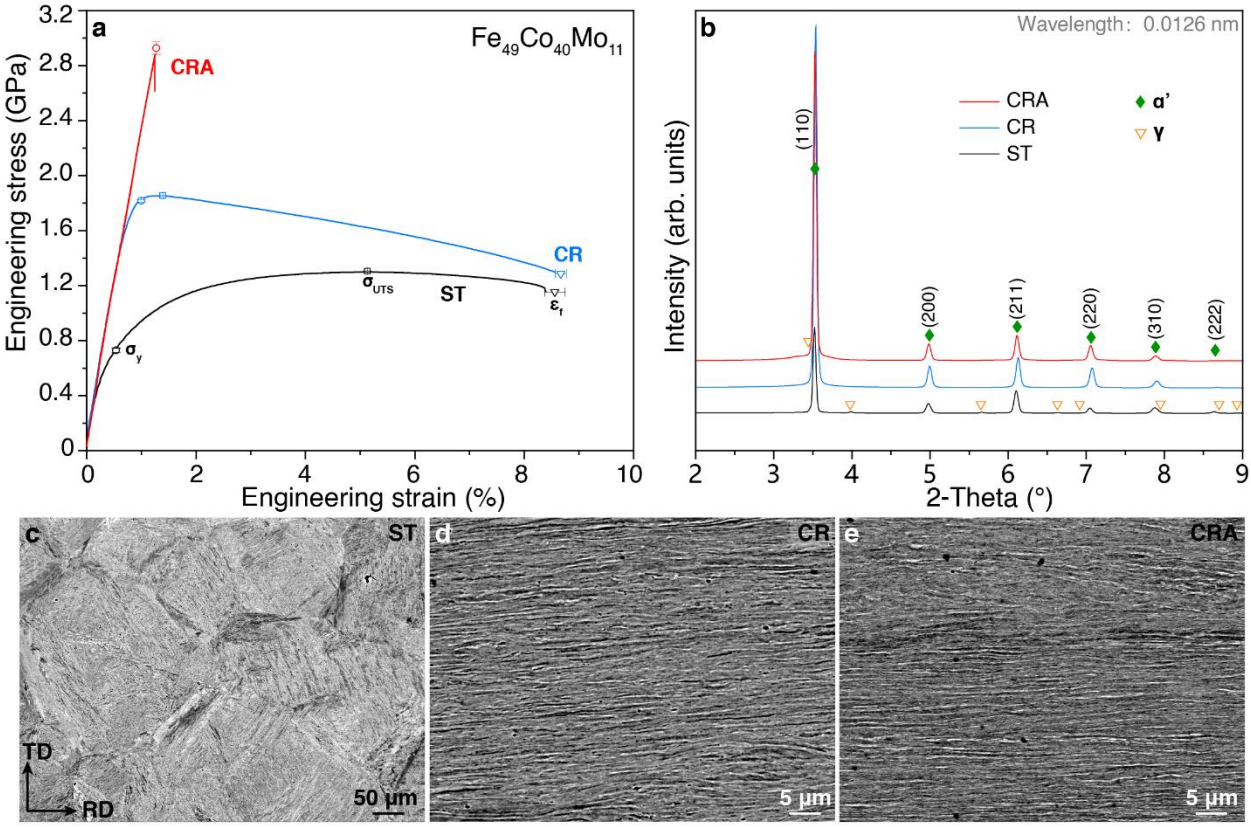

Supplementary Fig. 7 | Mechanical properties and microstructures of $Fe_{49}Co_{40}Mo_{11}$ alloy. a, Room-temperature engineering stress–strain curves showing that the CRA-treated alloy exhibits a high tensile strength of 2.92 GPa but limited ductility (~1%), with fracture occurring prior to macroscopic yielding. The data points and error bars represent the mean ± standard deviation (s.d.) taken from three independently tensile samples. **b,** HEXRD patterns reveal that the ST state contains both martensite and austenite phases, whereas the CR and CRA states are predominantly martensitic. **c-e,** SEM images of the ST, CR, and CRA conditions, respectively, indicating lath martensitic microstructures with no observable borides.

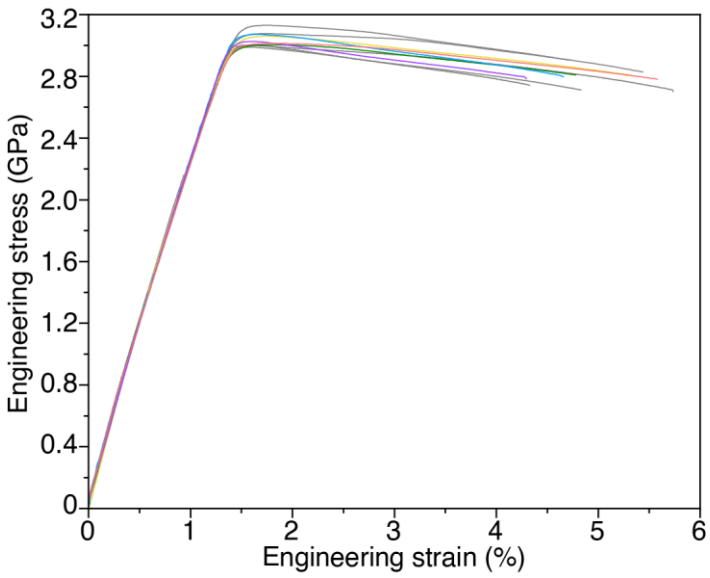

Supplementary Fig. 8 | Repeated tensile curves of the CRA-$(Fe_{49}Co_{40}Mo_{11})_{99.6}B_{0.3}C_{0.1}$ alloy. Ten room-temperature engineering stress–strain curves of the CRA alloy, demonstrating excellent reproducibility of its mechanical properties.

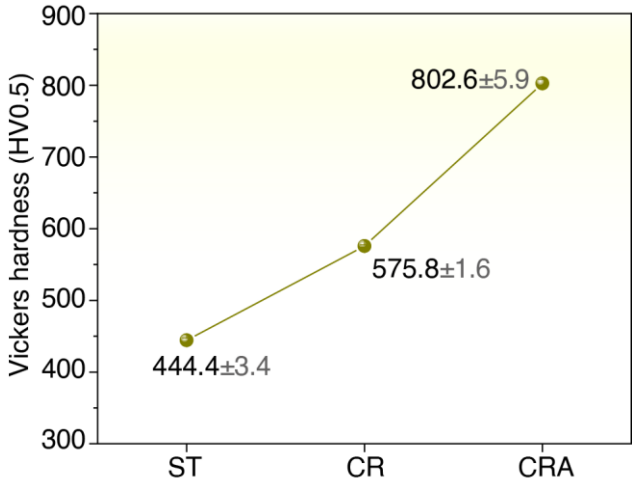

Supplementary Fig. 9 | Microhardness of the ST-, CR-, and CRA-$(Fe_{49}Co_{40}Mo_{11})_{99.6}B_{0.3}C_{0.1}$ alloys. The CRA alloy exhibits significantly higher microhardness compared to the ST and CR alloys. ST: homogenized at 1200 °C for 2 h; CR: 80% cold-rolled from the ST state; CRA: CR alloy subsequently annealed at 450 °C for 20 min. The data points and error bars represent the mean ± standard deviation (s.d.) taken from seven independently tests.

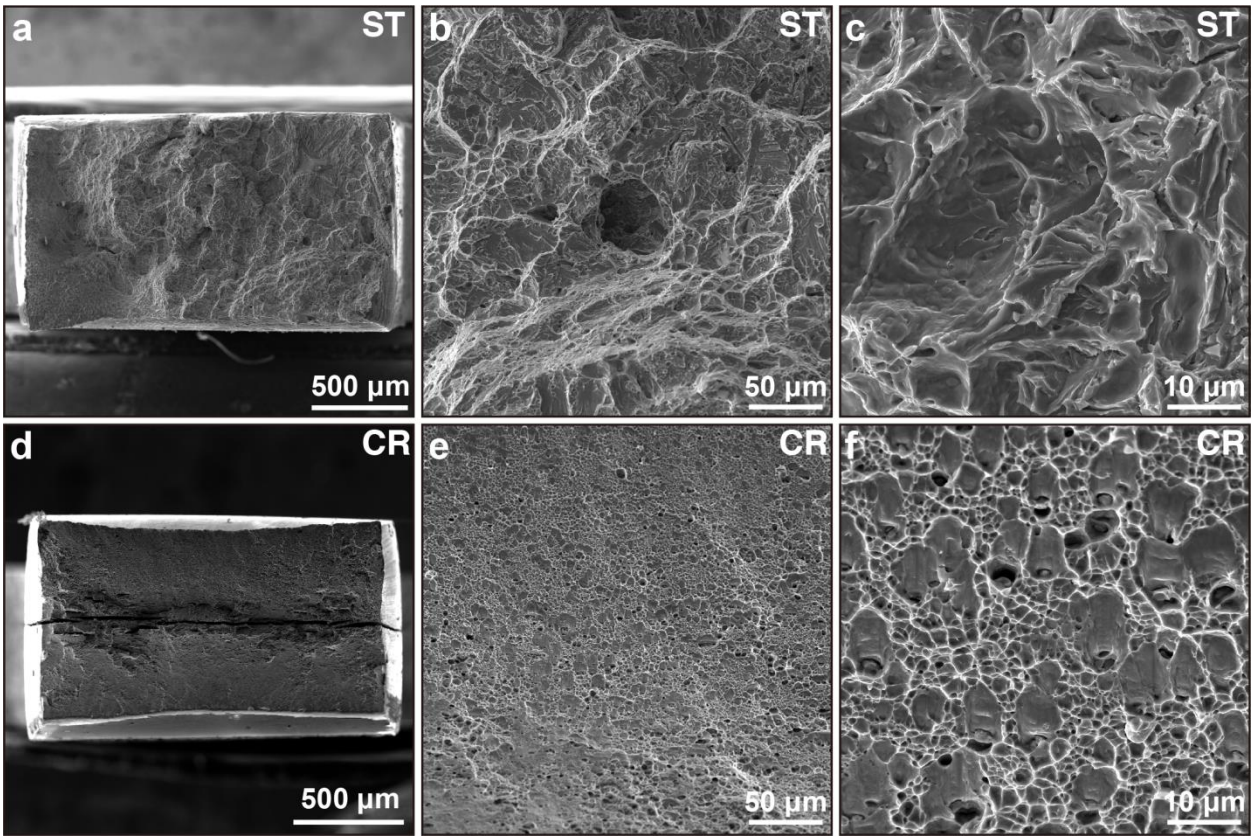

Supplementary Fig. 10 | Fracture morphologies of ST- and CR-$(Fe_{49}Co_{40}Mo_{11})_{99.6}B_{0.3}C_{0.1}$ alloys. Scanning electron microscope (SEM) images of fracture surfaces: **a-c,** ST alloy, displaying brittle fracture behavior characterized by abundant cleavage terraces, and **d-f,** CR alloy, exhibiting ductile fracture behavior with a dimpled surface.

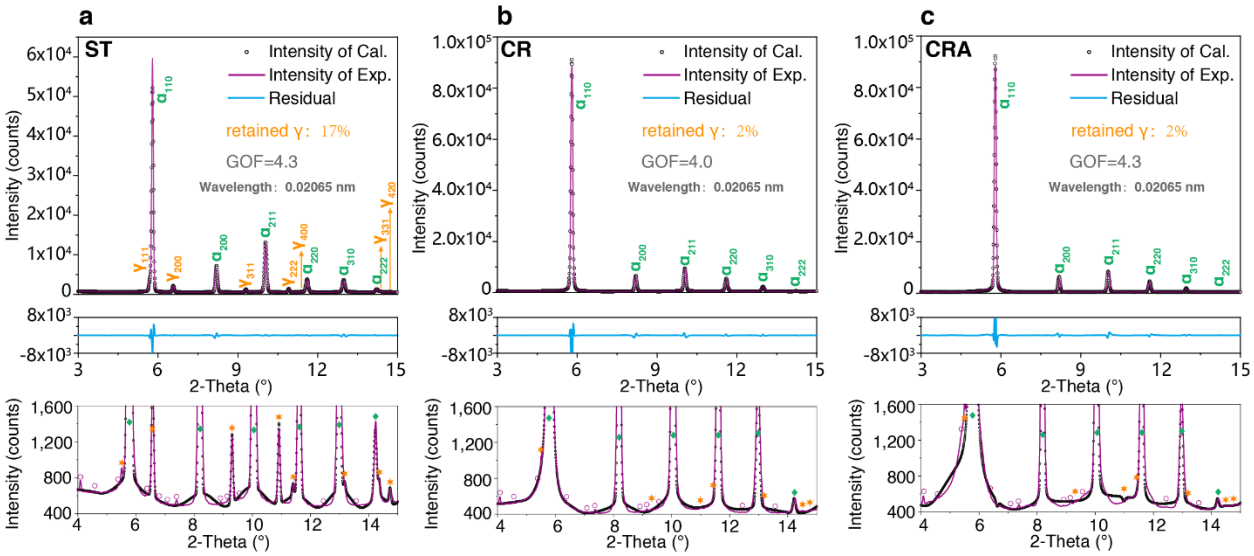

159

160 **Supplementary Fig. 11 | Rietveld refinement results.** Integrated diffraction profiles (solid lines)

161 of the ST, CR, and CRA alloys as a function of 2-theta, along with the corresponding fitted peaks

162 (open dots), obtained using the Rietveld refinement method. **a,** Refinement result for the ST alloy.

163 **b,** Refinement result for the CR alloy. **c,** Refinement result for the CRA alloy.

164 硼化物没有图注

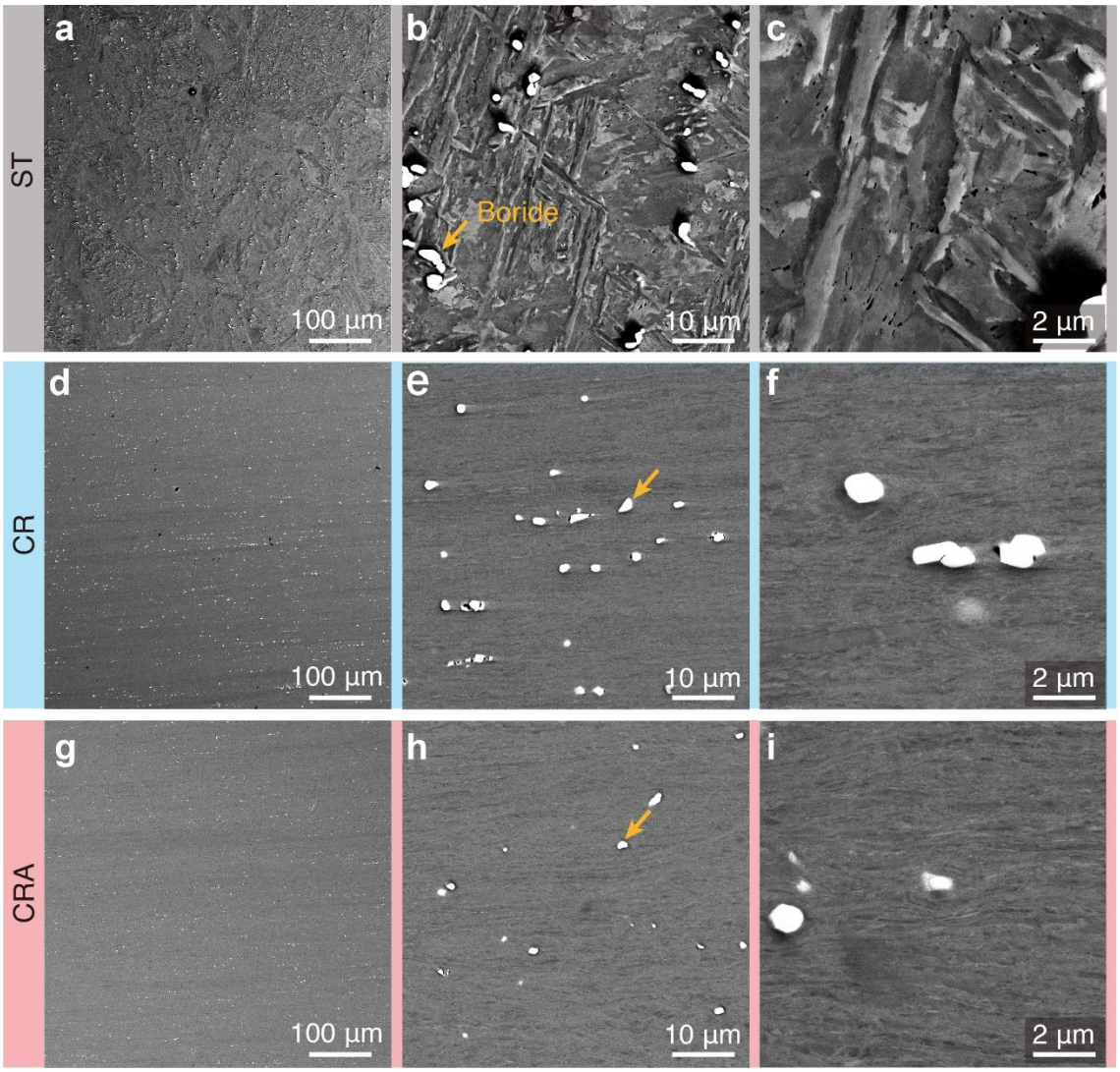

Supplementary Fig. 12 | Microstructures of the ST-, CR-, and CRA-$(Fe_{49}Co_{40}Mo_{11})_{99.6}B_{0.3}C_{0.1}$ alloys. SEM images showing the distribution of borides in **a-c,** the ST alloy, **d-f,** the CR alloy, and **g-i,** the CRA alloy. A sparse distribution of boride particles (marked by yellow arrows) is observed across the matrix for all three alloys.

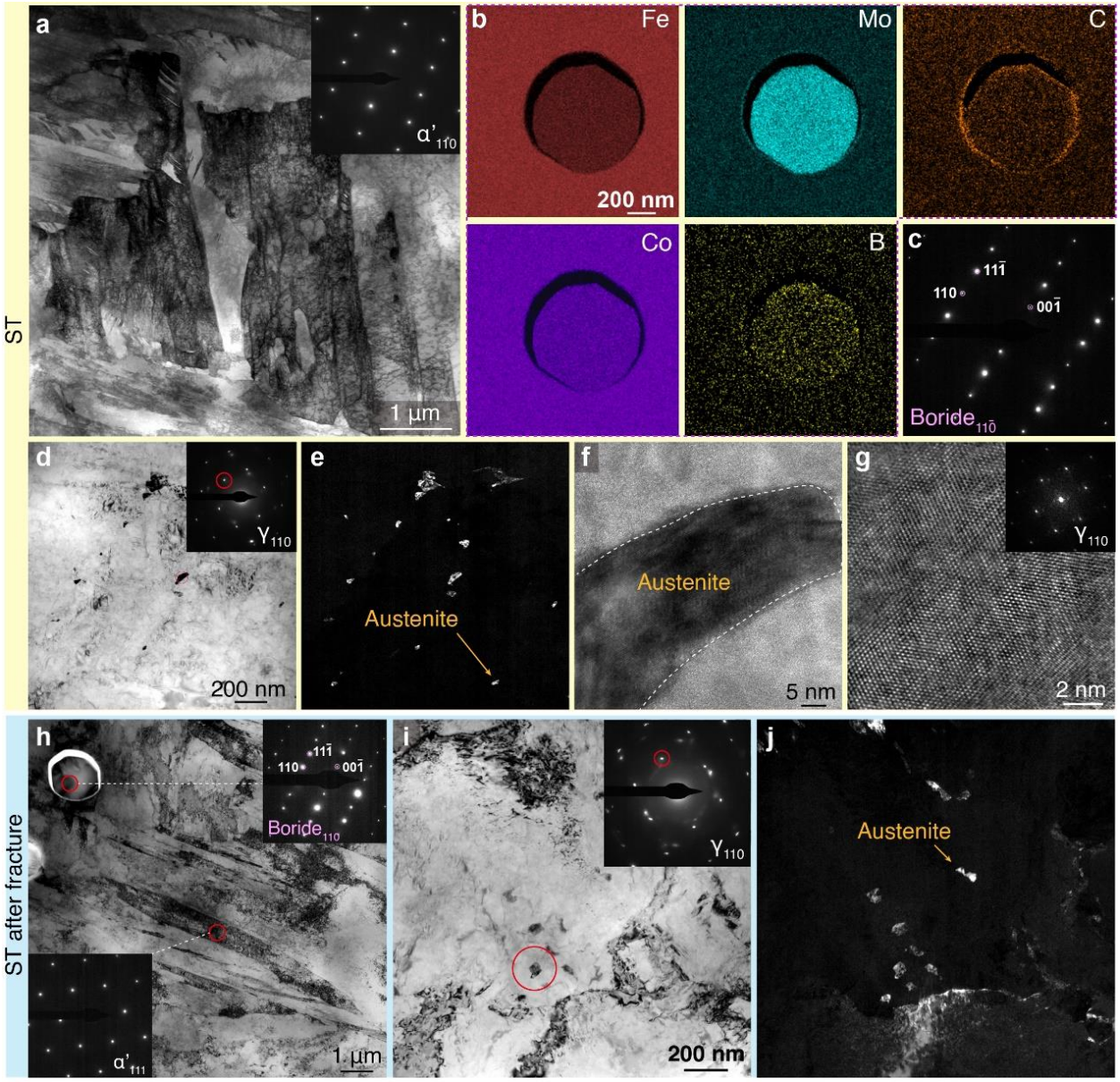

171

172 **Supplementary Fig. 13 | Microstructure of the ST-$(Fe_{49}Co_{40}Mo_{11})_{99.6}B_{0.3}C_{0.1}$ alloy before and**
173 **after tensile testing. a,** Bright-field TEM (BF-TEM) image before tensile testing, showing coarse
174 lath martensite boundaries; inset: selected-area electron diffraction (SAED) pattern confirming a
175 single body-centered cubic (bcc) martensite phase. **b**, **c**, TEM energy-dispersive spectroscopy
176 (EDS) and SAED patterns of boride particles, indicating Mo and B enrichment and hexagonal
177 close-packed structure. **d**, **e**, BF-TEM and dark-field TEM (DF-TEM) images of nanoscale
178 retained austenite. **f**, **g,** High-resolution TEM of austenite. **h**, BF-TEM after tensile fracture,
179 showing lath martensite matrix and boride particles. **i**, **j**, Corresponding BF-TEM and DF-TEM
180 images of retained austenite after fracture.

181

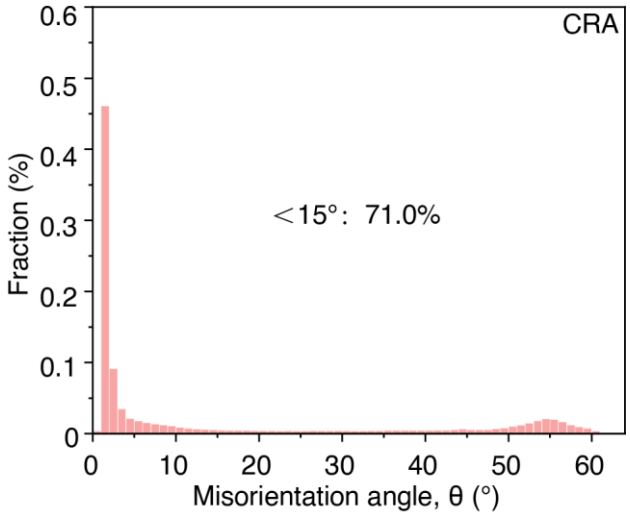

Supplementary Fig. 14 | Grain boundary misorientation. Distribution of grain boundary misorientation angles for the CRA alloy. A high density of small-angle grain boundaries (SAGBs) is present in the CRA alloy.

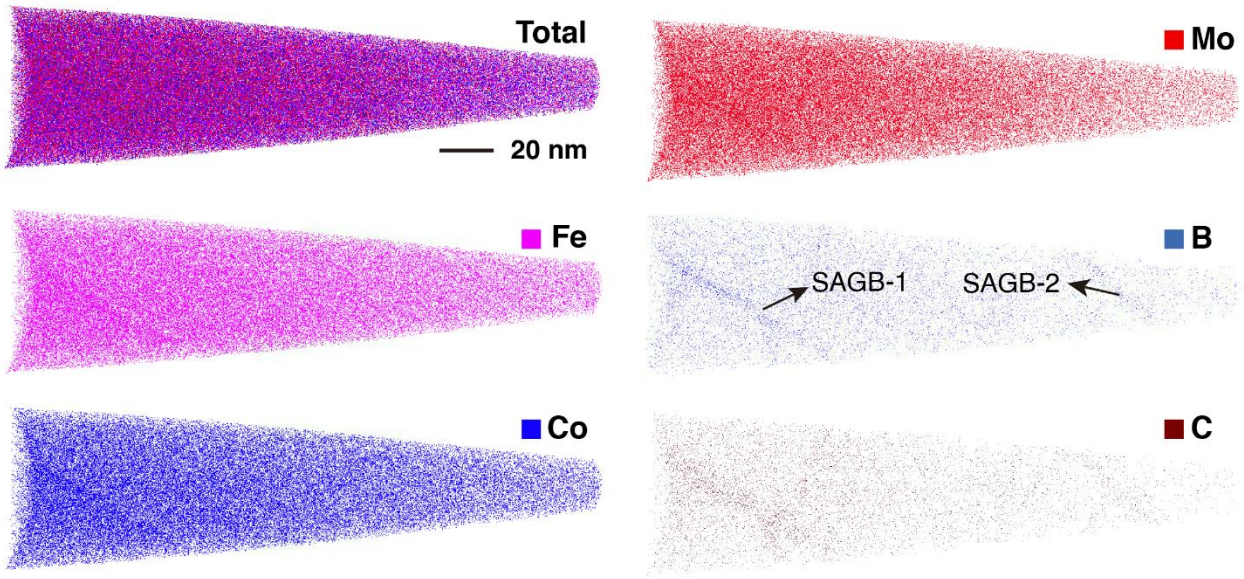

Supplementary Fig. 15 | Atom probe tomography measurements of the CRA alloy. The experimental dataset demonstrates the co-segregation of Mo, B, and C at SAGBs.

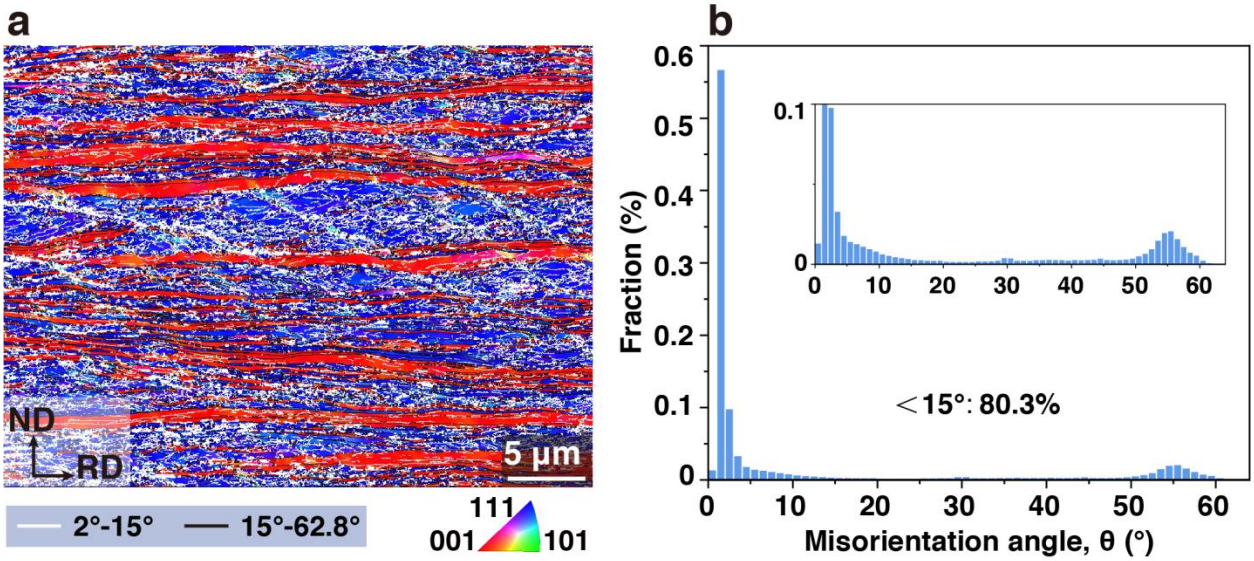

Supplementary Fig. 16 | High density of SAGBs in the CR alloy. a, Electron backscatter diffraction (EBSD) image along the ND-RD plane. **b,** Distribution of grain boundary misorientation angles. The planes along the rolling direction (RD) and normal direction (ND) are shown. The amount of SAGBs accounts for over 80 percent.

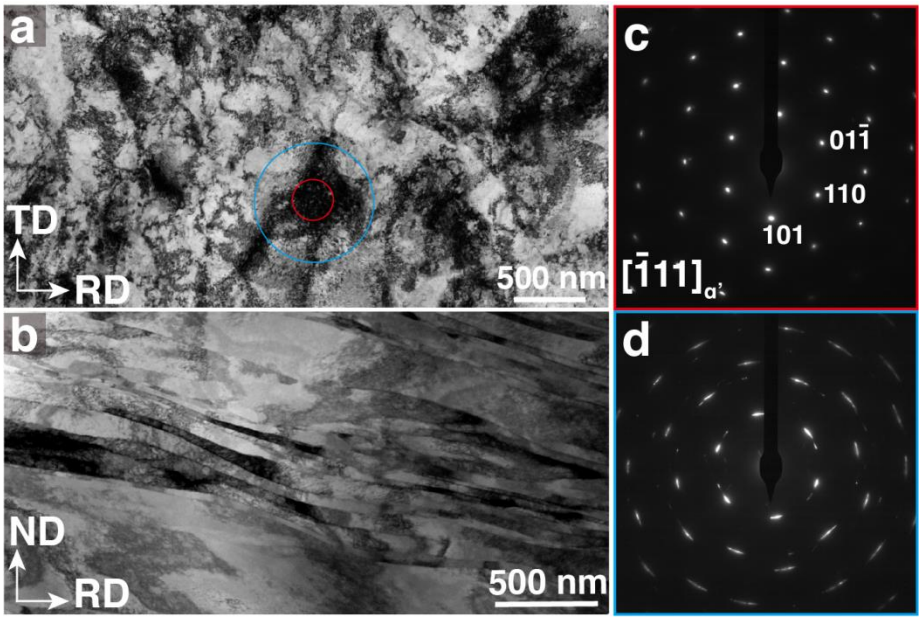

Supplementary Fig. 17 | Microstructure of the CR alloy. a, Bright-field transmission electron microscopy (TEM) image showing the massive subgrains microstructure on the TD-RD plane. **b,** Bright-field TEM image showing the lamellar microstructure on the ND-RD plane. **c** and **d,** Corresponding selected diffraction patterns for regions marked by red and blue solid circles in **a**, indicating a single martensite phase and high dislocation density within the matrix, respectively.

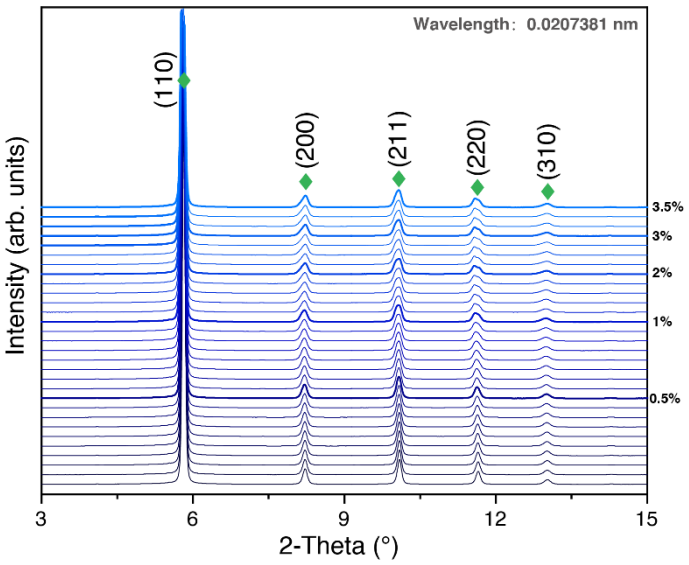

205

206 **Supplementary Fig. 18 | In-situ synchrotron high energy X-ray diffraction (HEXRD)**
207 **measurements.** *In-situ* synchrotron HEXRD profiles of the CR alloy obtained from the loading
208 direction at different tensile strains during deformation. The diffraction peaks broaden with the
209 increasing strain, indicating an increase in defect density.

210

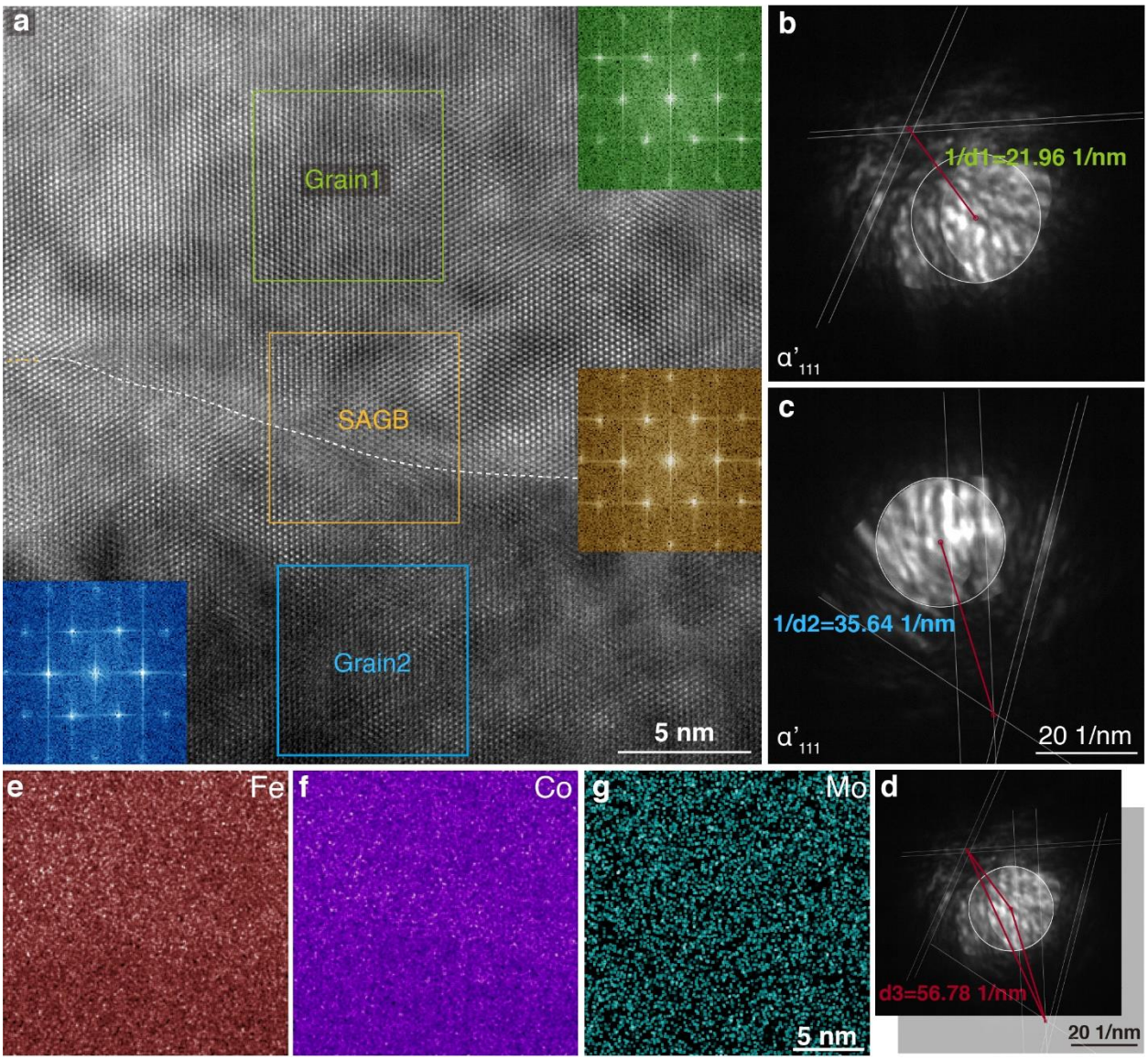

Supplementary Fig. 19 | Atomic-scale structure characterization of the CRA alloy. a, Aberration-corrected scanning transmission electron microscopy high-angle annular dark-field (STEM-HAADF) image with the incident beam aligned along the $[111]_{\alpha'}$ zone axis of a selected grain. **b**, **c**, Kikuchi patterns corresponding to two subgrains (Grain1 and Grain2), respectively. **d**, Superimposed Kikuchi patterns showing the intergranular center distance (d3) between the two grains; the misorientation angle between Grain1 and Grain2 was determined to be 8.2°. **e-g**, Corresponding STEM-EDS elemental maps of the region shown in **a**, revealing no detectable segregation or clustering.

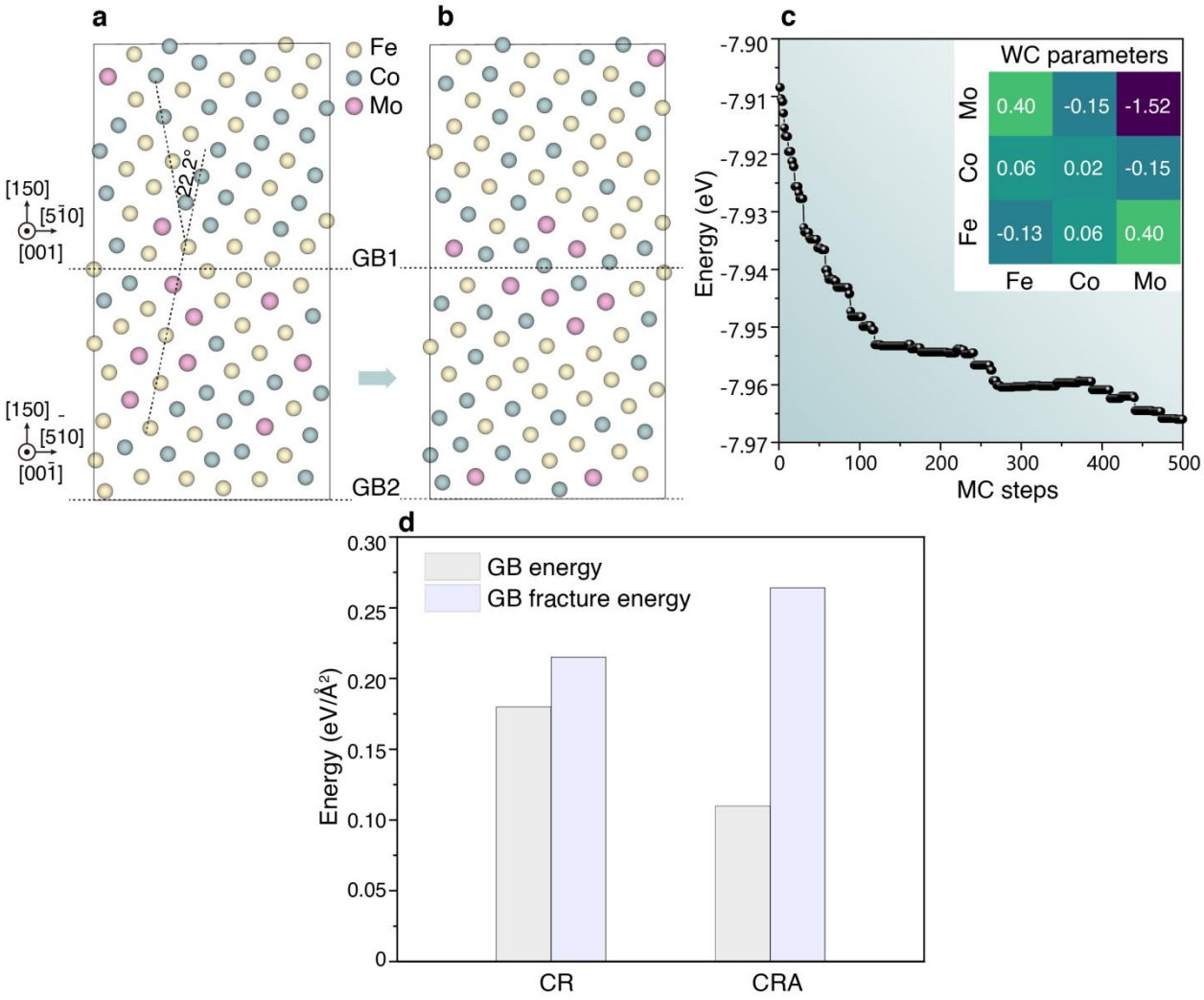

Supplementary Fig. 20 | Hybrid DFT/MC calculation results. Atomic structure of the [001](5$\bar{1}$0) and [00$\bar{1}$](5$\bar{1}$0) low-angle tilt grain boundaries **a,** before and **b,** after 500 MC swaps. **c,** Change in system energy with increasing MC steps. After 500 MC swaps, Mo segregation behavior and energy reduction are observed at the low-angle tilt boundaries. **d,** Grain boundary energy and grain boundary fracture energy of the CR and CRA alloys. The decrease in grain boundary energy and increase in grain boundary fracture energy after Mo segregation indicate enhanced grain boundary stability and cohesion, which contribute to improved yield strength and fracture resistance, respectively.

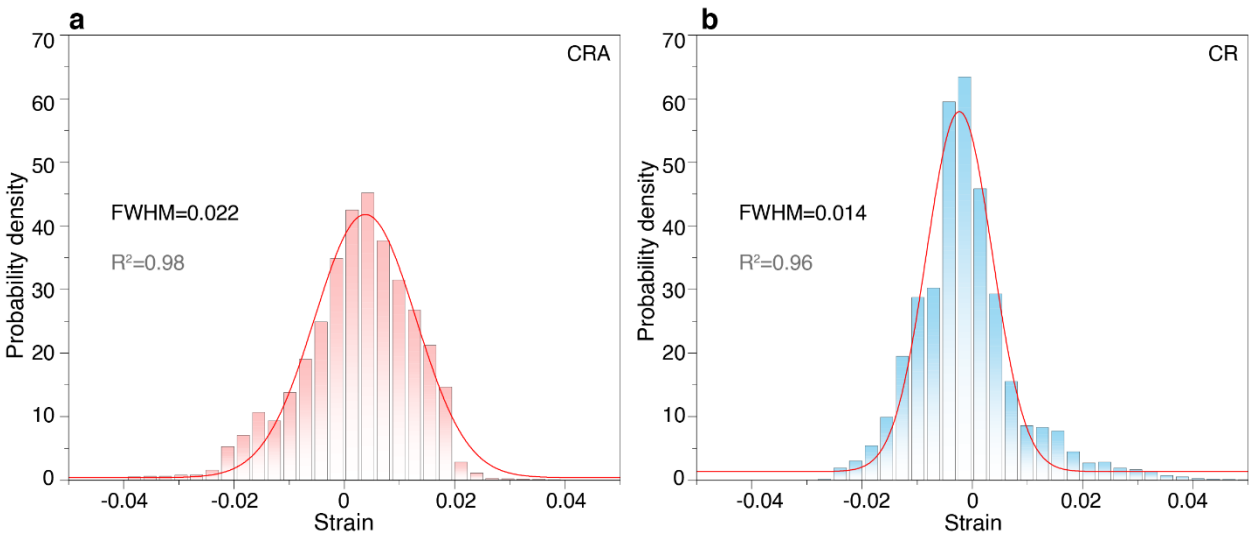

Supplementary Fig. 21 | Statistical results of the normal strain for discrete dislocation dynamics simulation and strain-field function. a, For the CRA alloy and **b,** for the CR alloy. The red solid line represents the Gaussian fitting curves of the strain-field histogram. The strain field distribution is broader in the CRA alloy, corresponding to larger FWHM value of the Gaussian.

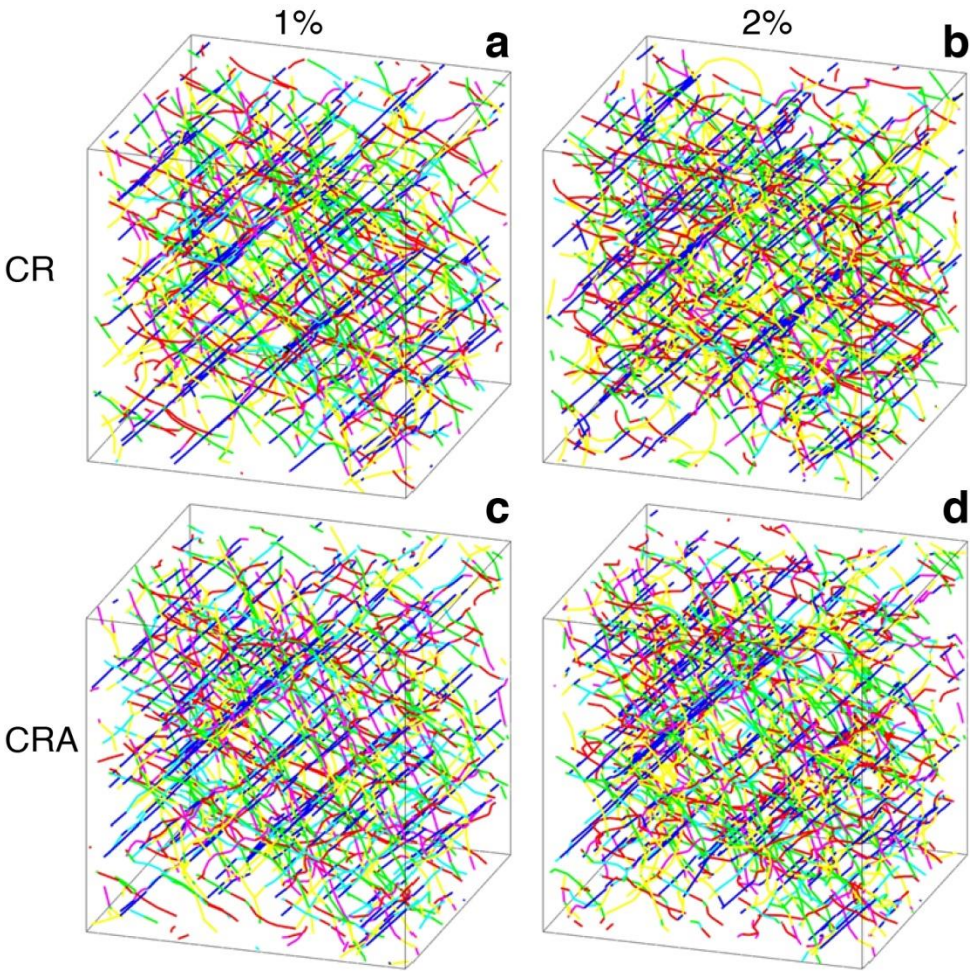

Supplementary Fig. 22 | Dislocation structure. Snapshots of the dislocation structure for the **a,** CR alloy at 1% strain, **b,** CR alloy at 2% strain, **c,** CRA alloy at 1% strain, and **d,** CRA alloy at 2% strain. Dislocations on the (110) slip plane are colored cyanine blue (——), the $(1\bar{1}0)$ slip plane is colored pinkish red (——), the (101) slip plane is colored yellow (——), the $(10\bar{1})$ slip plane is colored red (——), the (011) slip plane is colored green (——), and the $(01\bar{1})$ slip plane is colored blue (——).

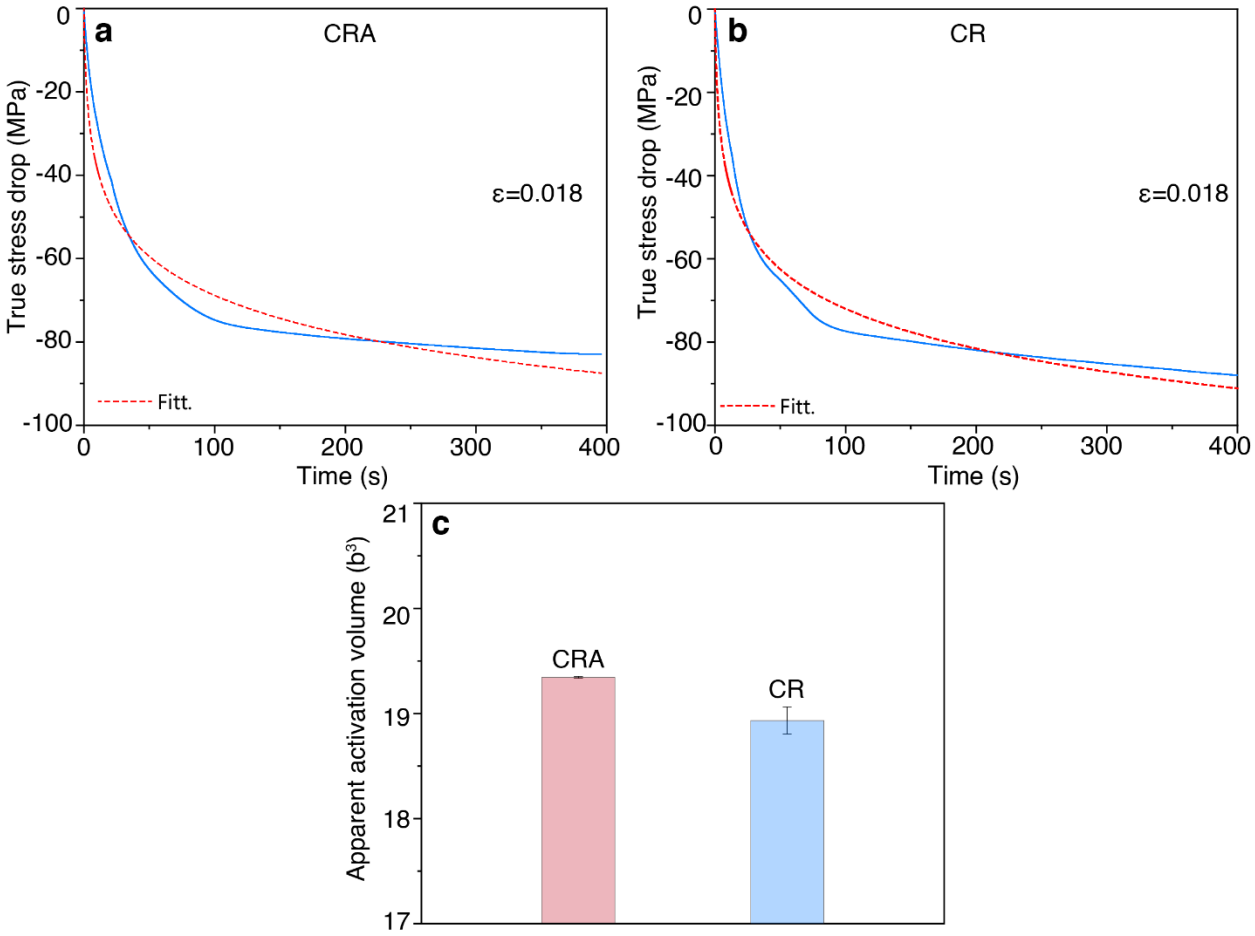

Supplementary Fig. 23 | Stress relaxation test. a-b, Stress relaxation processes at a true plastic strain of 0.018 in the CRA and CR alloys, respectively. **c,** Measured apparent activation volume of the CRA and CR alloys, with the apparent activation volume of the CRA alloy being slightly larger than that of the CR alloy. The data points and error bars represent the mean ± standard deviation (s.d.) taken from three independently tensile samples.

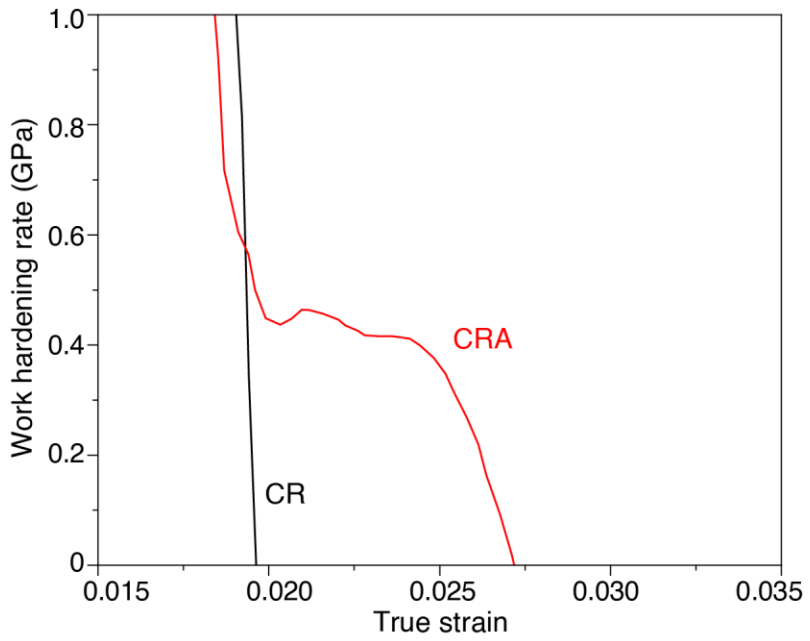

252

253 **Supplementary Fig. 24 | Work hardening rate as a function of true strain for the**
254 **$(Fe_{49}Co_{40}Mo_{11})_{99.6}B_{0.3}C_{0.1}$ alloy in CR and CRA states.** The CRA alloy exhibits a sustained
255 hardening plateau beginning near 2% strain, indicative of its superior dislocation storage capacity.

256

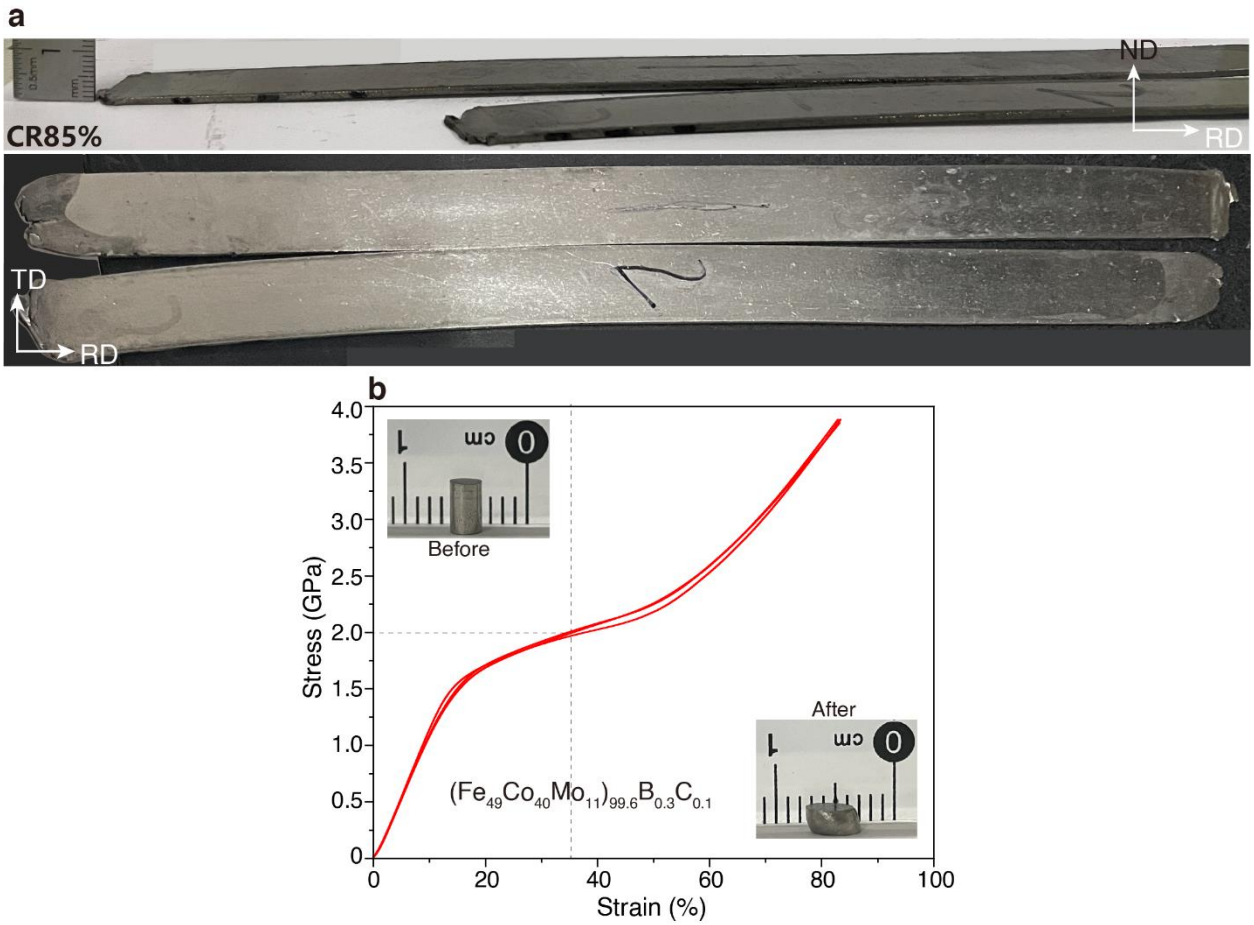

Supplementary Fig. 25 | Cold workability and mechanical properties of ST-$(Fe_{49}Co_{40}Mo_{11})_{99.6}B_{0.3}C_{0.1}$ at.% alloy. **a,** Real-time imaging during cold rolling. **b,** Compression engineering stress-strain curves. The tests were terminated at the 20 kN load limit. Three independent compression curves are presented to demonstrate the reproducibility and reliability of the experimental measurements.

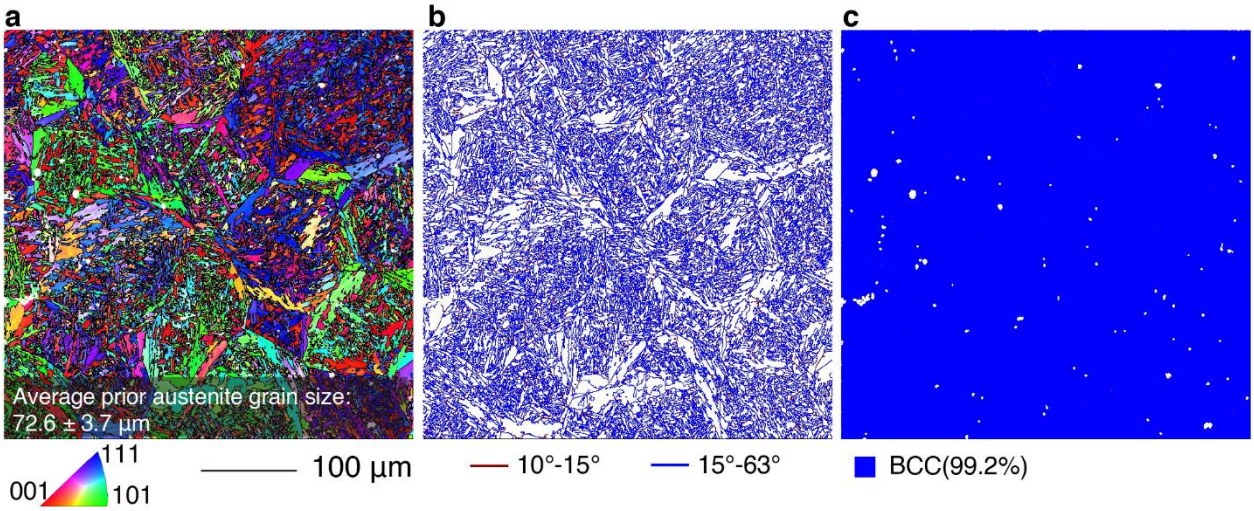

Supplementary Fig. 26 | Microstructural characterization of the $(Fe_{49}Co_{40}Mo_{11})_{99.6}B_{0.3}C_{0.1}$ alloy after 1200°C/2h solution treatment. a, EBSD-IPF maps. **b,** Boundary maps. **c,** Phase distribution diagrams. The average prior austenite grain size is 72.6 ± 3.7 μm.

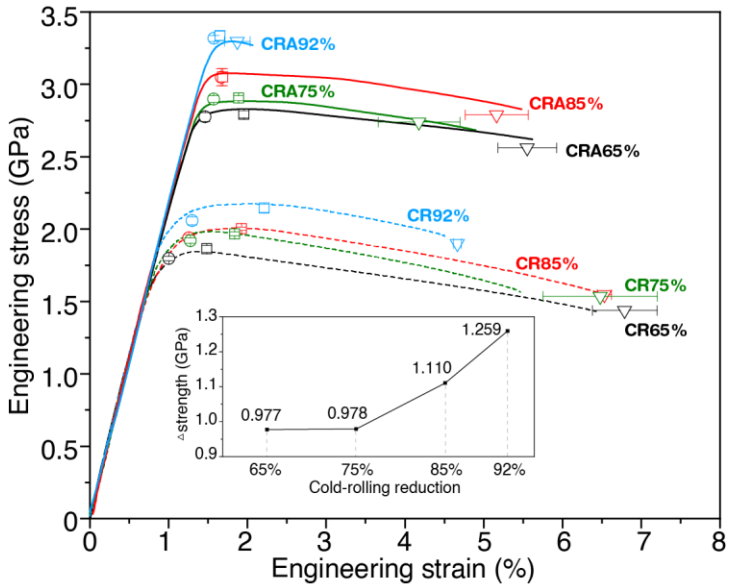

Supplementary Fig. 27 | Room-temperature tensile engineering stress-strain curves of the $(Fe_{49}Co_{40}Mo_{11})_{99.6}B_{0.3}C_{0.1}$ at.% alloy subjected to different cold-rolling reductions. The data points and error bars represent the mean ± standard deviation (s.d.) taken from three independently tensile samples.

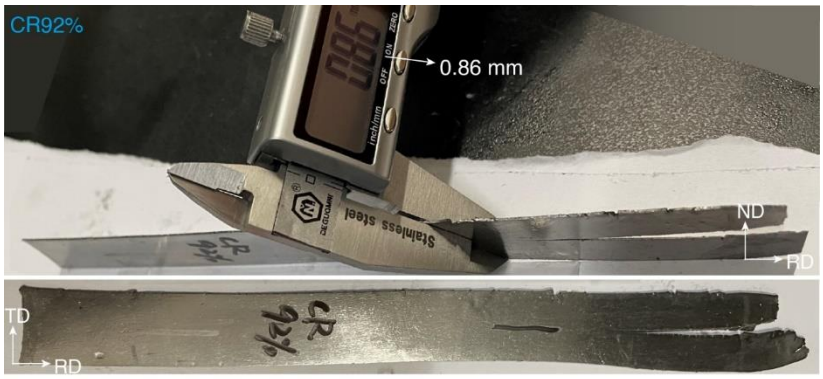

Supplementary Fig. 28 | Rolling plate of the $(Fe_{49}Co_{40}Mo_{11})_{99.6}B_{0.3}C_{0.1}$ alloy after 92% cold-rolling reduction, showing severe edge cracks.

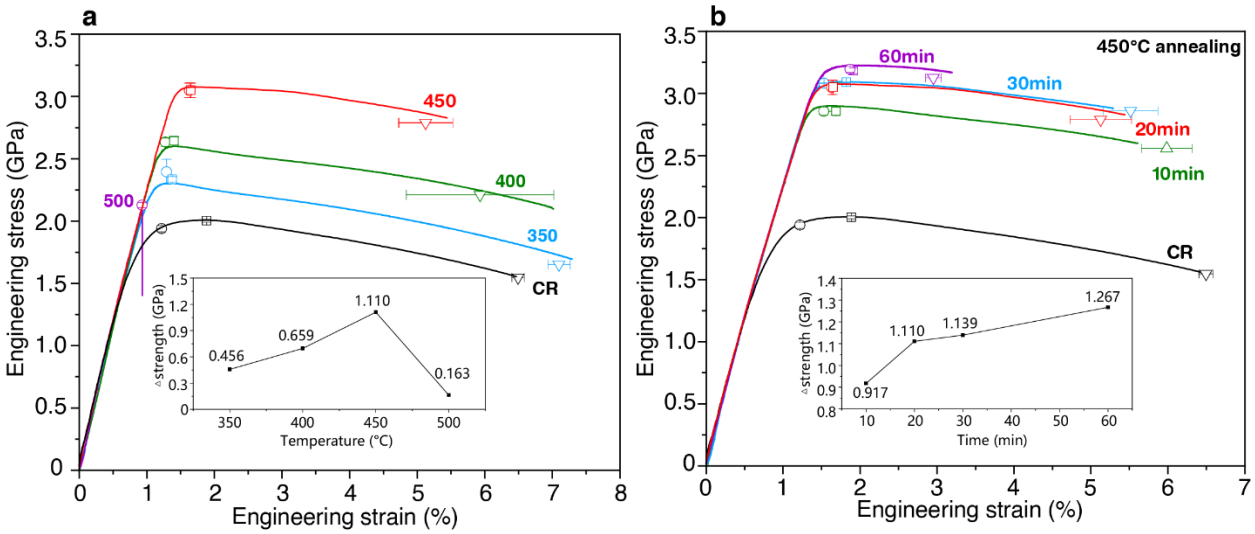

Supplementary Figs. 29 | Mechanical properties of the $(Fe_{49}Co_{40}Mo_{11})_{99.6}B_{0.3}C_{0.1}$ alloy after different processing. Room-temperature tensile engineering stress-strain curves of **a,** annealed for 20 min at different temperatures (350–500 °C), **b,** annealed at 450 °C for varying durations (10–60 min). The data points and error bars represent the mean ± standard deviation (s.d.) taken from three independently tensile samples.

Supplementary Table 1 Configurational entropy ΔS_{conf} and interface-complex strengthening for all investigated alloys. $\Delta\sigma_{\text{interface complexes}}$ denotes the yield strength enhancement from the CR to CRA state.

Alloy	ΔS_{conf}	$\Delta\sigma_{\text{interface complexes}}$ (GPa)
$(Fe_{55}Co_{40}Mo_5)_{99.6}B_{0.3}C_{0.1}$	1.002R	-
$(Fe_{53}Co_{40}Mo_7)_{99.6}B_{0.3}C_{0.1}$	1.044R	0.711
$(Fe_{51}Co_{40}Mo_9)_{99.6}B_{0.3}C_{0.1}$	1.080R	0.859
$(Fe_{49}Co_{40}Mo_{11})_{99.6}B_{0.3}C_{0.1}$	1.111R	1.110
$(Fe_{48}Co_{40}Mo_{12})_{99.6}B_{0.3}C_{0.1}$	1.125R	-
$(Fe_{47}Co_{40}Mo_{13})_{99.6}B_{0.3}C_{0.1}$	1.138R	-
$(Fe_{50}Co_{40}(TiVMoW)_{10})_{99.6}B_{0.3}C_{0.1}$	1.229R	0.643
$(Fe_{50}Co_{40}V_{10})_{99.6}B_{0.3}C_{0.1}$	1.096R	0.492
$(Fe_{60}Co_{25}Ni_{10}Mo_5)_{99.6}B_{0.3}C_{0.1}$	1.182R	0.680
$(Fe_{60}Co_{20}Ni_{15}Mo_5)_{99.6}B_{0.3}C_{0.1}$	1.211R	0.832
$(Fe_{54}Co_{35}Mo_{11})_{99.6}B_{0.3}C_{0.1}$	1.096R	-
$(Fe_{44}Co_{45}Mo_{11})_{99.6}B_{0.3}C_{0.1}$	1.115R	1.025
$(Fe_{39}Co_{50}Mo_{11})_{99.6}B_{0.3}C_{0.1}$	1.109R	-

Supplementary Table 2 Diffusion coefficients (*D*) of different elements. The table provides the diffusion coefficients *D* (in m^2/s) for various elements [20].

	Fe	Co	Mo	B	C
Intrinsic diffusion constant D_0 (1×10^{-4} m^2/s)	6.8	0.37	15.1	1.1×10^{-3}	2.0×10^{-2}
Activation energy for diffusion Q_D (kJ/mol)	258.9	280.5	216	72.4	84.098
Diffusion coefficient *D* (m^2/s)	1.3×10^{-22}	2.0×10^{-25}	3.7×10^{-19}	6.2×10^{-13}	1.7×10^{-12}
Reference	21	21	21	22	23

Supplementary Table 3 Mixing enthalpy values ($\Delta H^{\mathrm{mix}}_{\{\mathrm{AB}\}}$) of atomic pairs. The table presents the mixing enthalpy values (in kJ/mol) for various atomic pairs [24].

	Fe	Co	Mo
B	-26	-24	-34
C	-50	-42	-67

Supplementary References

1 Williamson, G. K. & Hall, W. H. X-ray line broadening from filed aluminium and wolfram. *Acta Metall.* **1**, 22-31 (1953).

2 Ungár, T., Dragomir, I., Révész, Á. & Borbély, A. The contrast factors of dislocations in cubic crystals: the dislocation model of strain anisotropy in practice. *J. Appl. Crystallogr.* **32**, 992-1002 (1999).

3 Zhang, H. et al. Single-crystal elastic constants of ferromagnetic bcc Fe-based random alloys from first-principles theory. *Phys. Rev. B* **81**, 184105 (2010).

4 Schoeck, G. Dislocation Theory of Plasticity of Metals. *Adv. Appl. Mech.* **4**, 229-279 (1956).

5 Arechabaleta, Z., van Liempt, P. & Sietsma, J. Unravelling dislocation networks in metals. *Mater. Sci. Eng. A* **710**, 329-333 (2018).

6 Liempt, P. v. & Sietsma, J. A physically based yield criterion I. Determination of the yield stress based on analysis of pre-yield dislocation behaviour. *Mater. Sci. Eng., A* **662**, 80-87 (2016).

7 Li, B. L. et al. Microstructural evolution of IF-steel during cold rolling. *Acta Mater.* **52**, 1069-1081 (2004).

8 Fleischer, R. L. Substitutional solution hardening. *Acta Metall.* **11**, 203-209 (1963).

9 Labusch, R. A Statistical Theory of Solid Solution Hardening. *Physica Status Solidi B* **41**, 659-669 (1970).

10 Niu, M. et al. Precipitate evolution and strengthening behavior during aging process in a 2.5 GPa grade maraging steel. *Acta Mater.* **179**, 296-307 (2019).

11 Taylor, G. I. The mechanism of plastic deformation of crystals. Part I.—Theoretical. *Proc. R. Soc. London, Ser. A* **145**, 362-387 (1934).

12 He, B. B. et al. High dislocation density–induced large ductility in deformed and partitioned steels. *Science* **357**, 1029–1032 (2017).

13 Sauzay, M. et al. Cyclic softening of martensitic steels at high temperature—Experiments and physically based modelling. *Mater. Sci. Eng. A* **483-484**, 410-414 (2008).

14 Ungár, T., Stoica, A. D., Tichy, G. & Wang, X.-L. Orientation-dependent evolution of the dislocation density in grain populations with different crystallographic orientations relative to the tensile axis in a polycrystalline aggregate of stainless steel. *Acta Mater.* **66**, 251-261 (2014).

15 Huang, X., Morito, S., Hansen, N. & Maki, T. Ultrafine Structure and High Strength in Cold-Rolled Martensite. *Metall. Mater. Trans. A* **43**, 3517-3531 (2012).

16 Speich, G. R. & Leslie, W. C. Elastic Constants of Martensite. *Mater. Trans.* **4**, 1973-1873 (1973).

17 Hall, E. The deformation and ageing of mild steel: III discussion of results. *Proc. Phys. Soc. London, Sect. B* **64**, 747 (1951).

18 Petch, N. J. The cleavage strength of polycrystals. *J. Iron Steel Inst.* **174**, 25-28 (1953).

19 Li, M., Peng, Z., Shang, Y. & Liu, Y. Phase Equilibria in the Fe-Mo-Co System: Experimental Investigation and Thermodynamic Calculation. *Coatings* **13**, 1215 (2023).

20 Huang, Y. C., Lai, Y. C., Lin, Y. H. & Wu, S. K. A study on the severely cold-rolled and annealed quaternary equiatomic derivatives from quinary HfNbTaTiZr refractory high entropy alloy. *J. Alloys Compd.* **855**, 157404 (2021).

21 Gerhard, N. & Tuijn, C. Self-diffusion and impurity diffusion in pure metals: handbook of experimental data. Vol. 14 (2011).
22 Li, X. et al. Boron diffusion in bcc-Fe studied by first-principles calculations. *Chin. Phys. B* **25**, 036601 (2016).
23 Wert, C. A. Diffusion Coefficient of C in α-Iron. *Phys. Rev.* **79**, 601-605 (1950).
24 Takeuchi, A. & Inoue, A. Classification of bulk metallic glasses by atomic size difference, heat of mixing and period of constituent elements and its application to characterization of the main alloying element. *Mater. Trans.* **46**, 2817-2829 (2005).